crystals

MDPI

Article

Preliminary Serial Femtosecond Crystallography Studies of Myoglobin from Equine Skeletal Muscle

Jaehyun Park [1,*], Sehan Park [1] and Ki Hyun Nam [2,*]

[1] Pohang Accelerator Laboratory, Pohang University of Science and Technology, Pohang 37673, Republic of Korea
[2] College of General Education, Kookmin University, Seoul 02707, Republic of Korea
* Correspondence: jaehyun.park@postech.ac.kr (J.P.); structure@kookmin.ac.kr (K.H.N.)

Abstract

Myoglobin (Mb), a heme-containing protein, plays crucial roles in storing and transporting oxygen in muscle cells. Various Mb structures have been extensively determined using conventional cryogenic crystallography, providing valuable information for understanding the molecular mechanisms of the protein. However, this approach has limitations attributable to cryogenic temperatures and radiation damage. Serial femtosecond crystallography (SFX) using X-ray free-electron lasers is an emerging technique that enables the determination of biologically relevant room-temperature structures without causing radiation damage. In this study, we assessed the crystallization, collection, and processing of SFX diffraction data of Mb from equine skeletal muscle. Needle- and needle cluster-shaped Mb crystals were obtained using the microbatch method. Fixed-target SFX data collection was performed at the Pohang Accelerator Laboratory X-ray Free Electron Laser, yielding 1389 indexed diffraction patterns. The phase problem was solved by molecular replacement. The preliminary Mb structure determined at 2.3-Å resolution in this study exhibited subtle structural differences in the heme environment compared with previously reported Mb structures determined by SFX. These results both confirm the feasibility of myoglobin SFX experiments and establish a foundation for future time-resolved studies aiming to visualize ligand binding and oxygen transport.

Keywords: myoglobin; serial femtosecond crystallography; PAL-XFEL

check for updates

Academic Editor: Abel Moreno

Received: 3 October 2025
Revised: 16 October 2025
Accepted: 17 October 2025
Published: 18 October 2025

Citation: Park, J.; Park, S.; Nam, K.H. Preliminary Serial Femtosecond Crystallography Studies of Myoglobin from Equine Skeletal Muscle. *Crystals* **2025**, *15*, 905. https://doi.org/10.3390/cryst15100905

Copyright: © 2025 by the authors. Licensee MDPI, Basel, Switzerland. This article is an open access article distributed under the terms and conditions of the Creative Commons Attribution (CC BY) license (https://creativecommons.org/licenses/by/4.0/).

1. Introduction

Myoglobin (Mb) is a heme protein found in the muscle tissues of vertebrates, in which it functions in oxygen storage and transport [1,2]. In addition, Mb regulates nitric oxide signaling [3]. In 1960, Mb became the first protein with a determined three-dimensional structure [4]. The molecular properties and functions of Mb have been extensively investigated. Mb is widely applied in the food industry to impart characteristic color and flavor into plant-based meat products [5,6], and it has also been utilized as a diagnostic marker of muscle injury [7].

Over recent decades, various crystal structures of Mb have been determined, contributing to both the clarification of Mb function and broader advances in protein science [8–11]. In particular, studies on ligand binding, protein dynamics, and allosteric conformational changes in Mb have provided fundamental insights into biophysical concepts [11–14]. However, most of these structures were determined using traditional X-ray crystallography under cryogenic conditions, which carry experimental limitations related to cryogenic

temperature and radiation damage [15–20]. These limitations hinder the ability to capture the intrinsic flexibility of Mb, including conformational distributions and the sensitivity of the iron-centered heme group to radiation damage [21,22].

Serial femtosecond crystallography (SFX) with an X-ray free-electron laser (XFEL) represents an alternative method to overcome the aforementioned limitations of conventional crystallography [23,24]. SFX enables the determination of room-temperature structures while minimizing radiation damage based on the "diffraction before destruction" principle [25,26]. Moreover, SFX combined with pump–probe experiments using an optical laser or with mix-and-inject approaches enables the determination of time-resolved (TR) molecular dynamics during the photoreaction or enzymatic reaction [27–29]. In SFX studies, Mb has been used as a model system for TR experiments [30,31] and as a model sample for SX methodology development [32–35]. In particular, a TR-SFX experiment demonstrated that photolysis of the Fe–CO bond in carboxymyoglobin induces helices surrounding the heme to move within 500 fs [30]. However, more recent studies found that the photodissociation dynamics of carboxymyoglobin are affected by pump laser fluence, highlighting the need to reassess both the design and interpretation of ultrafast TR-SFX experiments [31].

Mb can exist in various functional states, such as deoxy-Mb (ligand-free), oxy-Mb (O_2-bound), carboxy-Mb (CO-bound), and multiple oxidation states of the heme molecule in Mb [36,37], but these states have not yet been fully characterized in SFX studies. To better understand the molecular function of Mb, it is important to perform TR-SFX studies of these functional states of Mb and examine the conformational flexibility of the protein at room temperature.

In this study, we report the crystallization and XFEL diffraction data collection of Mb from equine skeletal muscle. The XFEL data were collected using a fixed-target scanning method at Pohang Accelerator Laboratory X-ray Free Electron Laser (PAL-XFEL). Our preliminary XFEL structure of Mb was compared with previously reported Mb structures determined by SFX. These results provide useful information for sample preparation and data processing in future TR-SFX studies of Mb.

2. Materials and Methods

2.1. Crystallization

Mb from equine skeletal muscle was purchased from Sigma-Aldrich (St. Louis, MO, USA; Cat. No. M0630). Mb powder was dissolved at a concentration of 30–100 mg/mL in 10 mM Tris-HCl (pH 8.0) and 50 mM NaCl. Crystallization was performed by the batch method in a microtube [38]. The protein solution (100 µL) was mixed with crystallization solution (400 µL) containing 2–4 M ammonium sulfate. The mixture was vortexed at 4000 rpm for 1 min and then stored in a 20 °C incubator. Needle- and needle cluster-shaped Mb crystals grew within 2 weeks.

2.2. Sample Preparation for the Fixed-Target Scan

Mb crystals were delivered to the X-ray region using a nylon mesh-based sample holder with dimensions of 20 × 20 mm^2 [39]. Brownish Mb crystals were harvested in a microtube. A total of 440 µL of crystallization solution positioned above the settled crystals was removed using a pipette. The remaining 60 µL of the sample were gently resuspended with a pipette. Crystal suspensions were transferred onto the nylon mesh (pore size: 60 µm) supported by a polyimide film (25 µm) frame and spread with a pipette tip. To reduce the X-ray background signal from the crystallization solution, 20 µL of the solution was carefully removed from the deposited crystal suspension on the nylon mesh. To prevent evaporation of the crystallization solution, the Mb crystal suspension was immediately

covered with an additional polyimide film (25 μm) frame. The sample holder containing the Mb crystals was stored at room temperature until data collection.

2.3. XFEL Data Collection

SFX experiments were performed at the Nano Crystallography and Coherence Imaging (NCI) endstation [40] at PAL-XFEL (Pohang, Republic of Korea) [41]. The X-ray pulse energy was 9500 eV (wavelength: 1.3051 Å) with a pulse width of approximately 20 fs. The XFEL operated at a repetition rate of 30 Hz, delivering approximately 2×10^{11}–3×10^{11} photons per pulse. The X-ray beam was focused using a Kirkpatrick–Baez mirror system [42], and the beam size at the sample position was approximately 3×3 μm^2 (horizontal × vertical, full width at half-maximum). The sample holder containing the Mb crystals was mounted on the fixed-target translation stage and raster-scanned at 50-μm intervals in horizontal and vertical directions from top to bottom. The stage was moved at a velocity of 1.5 mm/s in both horizontal and vertical directions. Diffraction data were collected in an atmosphere at room temperature and recorded on an MX225-HS detector (Rayonix, LLC, Evanston, IL, USA) with 4 × 4 binning (pixel size: 156 μm × 156 μm). The diffraction peaks from the collected images were monitored in real time using the OnDA program during data collection [43].

2.4. Data Processing

Hit images containing Bragg peaks were filtered using Cheetah [44]. The hit images were further processed using CrystFEL (Version 0.9.1+886ae521) [45]. Peaks were detected using the peakfinder8 algorithm, and diffraction patterns were indexed using XGANDALF algorithm [46]. Detector geometry was optimized using geoptimiser [47] during data processing. Indexed images were scaled with partialator implemented in CrystFEL.

2.5. Initial Structure Determination

The phasing problem was solved by molecular replacement (MR) using Phaser-MR implemented in PHENIX (Version 1.17.1_3660) [48]. The crystal structure of Mb (PDB ID: 1AZI) [49] was used as the search model. The model structure was manually built using COOT (0.9.8.95) [50]. Structure refinement was performed using phenix.refine in PHENIX. The geometry of the final model was validated by MolProbity [51]. Structure figures were generated by PyMOL (https://www.pymol.org/; accessed on 25 August 2025).

3. Results

3.1. Mb Crystallization

In SFX experiments, each crystal is exposed to a single XFEL pulse only once, and the resulting data are free from cumulative radiation damage. As each exposure yields only partial diffraction information, a large number of crystals is essentially required to determine the complete three-dimensional structure. To obtain sufficient quantities of Mb crystals, we performed batch crystallization in microtubes at room temperature. Crystal nucleation, which is closely correlated with both the number and size of crystals, is generally affected by the protein solution and precipitant concentrations. Accordingly, Mb crystallization trials were conducted under various protein (30, 50, and 100 mg/mL) and precipitant concentrations (2, 3, and 4 M ammonium sulfate). Among the various conditions, brownish material settled at the bottom of the microtubes in samples containing 50 mg/mL protein and 3–4 M precipitant (Figure 1A). Because the heme group in myoglobin contains iron, it imparts a characteristic brownish color to the protein, indicating that most Mb molecules were incorporated into the crystals. However, a faint brown tint was also observed in the supernatant, suggesting that a small fraction of Mb remained

soluble rather than contributing to crystallization. Microscopic observation revealed needle-shaped or clustered Mb crystals with a typical crystal width of <3 μm (Figure 1B). The lengths of needle-shaped single crystals ranged from a few micrometers to several tens of micrometers. In contrast, crystals within needle clusters appeared relatively thicker and longer; however, these were overlapping aggregates of multiple needles rather than true single crystals. These observations suggest that batch crystallization in microtubes promotes numerous nucleation events, leading to the formation of a large number of crystals. Nevertheless, the sizes and morphologies of the crystals produced under these conditions were highly heterogeneous. As a result, the diffraction intensities of individual crystals were inconsistent, and in the case of needle cluster samples, the overlapping nature of multiple needles likely gave rise to multi-crystal diffraction patterns. At a protein concentration of 100 mg/mL, brownish material was also observed in the microtubes, yet no well-defined crystalline morphology could be detected under microscopic inspection. This indicates that excessively high protein concentrations promoted uncontrolled nucleation or aggregation, thereby preventing the growth of well-ordered crystals.

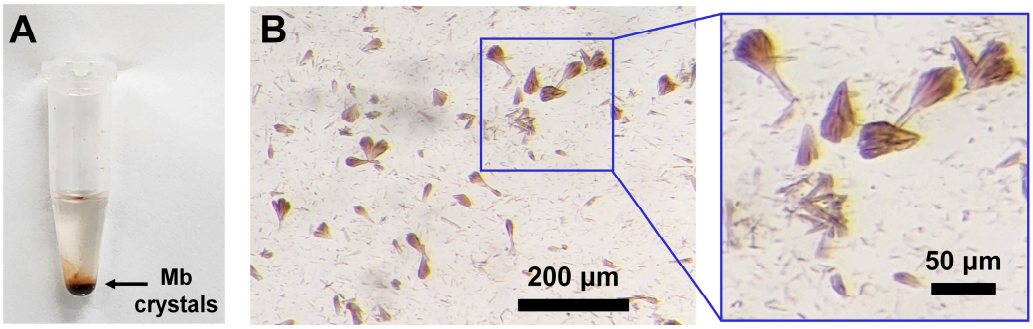


Figure 1. Photographs of Mb microcrystals used in this XFEL study. (**A**) Mb crystals in a microtube as obtained by the batch crystallization method. (**B**) Microscopic images of Mb crystals. The right panel presents a magnified view of the boxed region.

3.2. XFEL Data Processing for Mb

Initial X-ray diffraction analysis of these Mb crystals was performed at room temperature using synchrotron X-ray at PAL; however, no reliable diffraction patterns were obtained. The same crystal samples were then subjected to XFEL diffraction at PAL-XFEL. Mb crystals were delivered into the X-ray interaction region using a fixed-target scanning method. To avoid radiation damage, raster scanning was conducted at 50-μm intervals, exceeding the XFEL beam size of 3 μm (full width at half-maximum), in both horizontal and vertical directions. In total, 130,665 XFEL images were collected for 1.2 h, and 70,195 hit mages were obtained. The indexing efficiency of diffraction patterns can vary depending on the algorithm used [52,53]. Accordingly, various indexing algorithms, including MOSFLM, XDS, DirAx, and XGANDALF, were tested for data processing. Among these, XGANDALF produced the highest number of indexed patterns, yielding 1389 diffraction patterns from 1376 indexed images. Meanwhile, MOSFLM, XDS, and DirAx indexed only 53, 13, and 210 images, respectively, resulting in incomplete datasets. Although all available algorithms were applied to maximize the number of indexed diffraction patterns, the overall data quality was poorer than that achieved using XGANDALF alone. Therefore, only the XGANDALF algorithm was applied for subsequent data processing. Image analysis confirmed that the diffraction peaks were correctly indexed at the predicted positions (Figure 2A). The unit cell parameter distribution of the processed Mb data exhibited Gaussian profiles for the a, b, and c axes and the α, β, and γ angles (Figure 2B). The Mb crystals belonged to the monoclinic space group $P2_1$ and featured the following unit cell dimensions: a = 63.95 Å, b = 28.62 Å, c = 35.59 Å, α = 90.00°, β = 107.19°, and γ = 90.00°. The Matthews coefficient

was calculated as 1.86 Å^3/Da with a solvent content of 34.03%, consistent with one molecule per asymmetric unit.

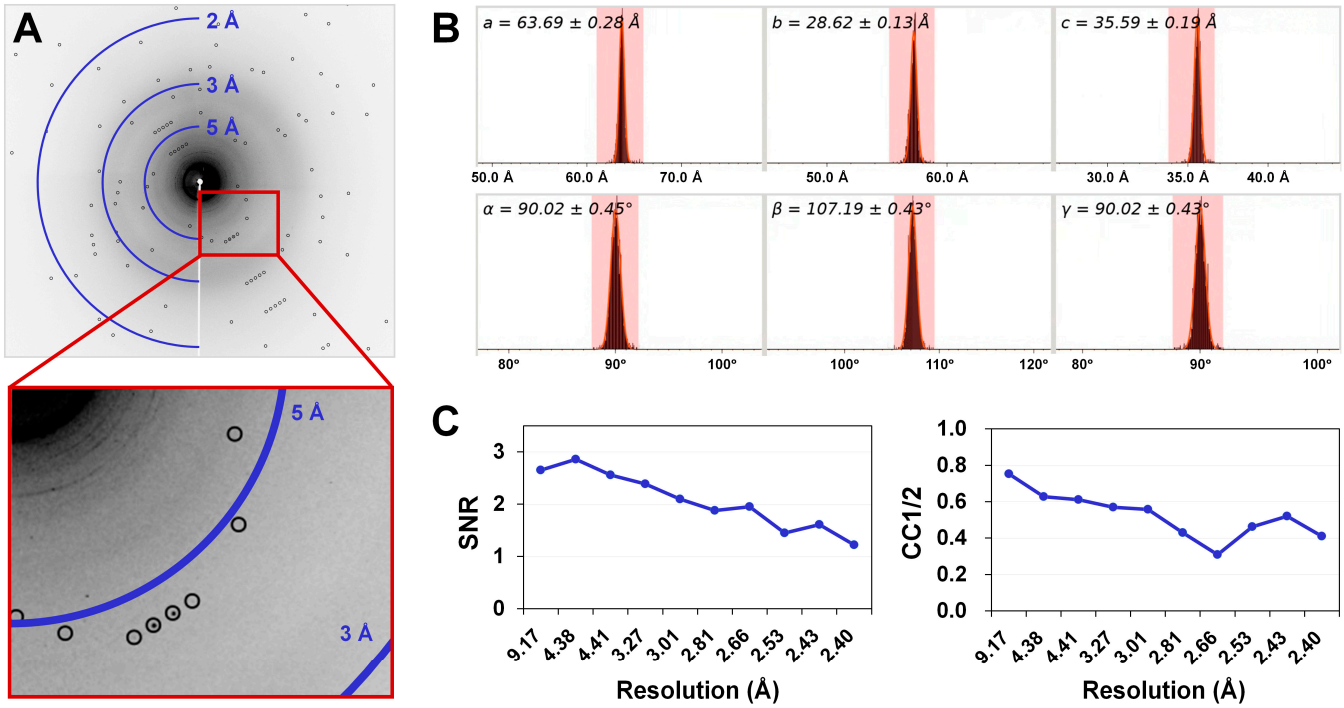


Figure 2. XFEL data collection and processing for Mb. (**A**) XFEL diffraction pattern of Mb. Circles indicate the predicted indexing positions. (**B**) Unit cell distribution of processed XFEL images of Mb. (**C**) Profiles of SNR and CC1/2 statistics for Mb across resolution ranges.

The XFEL diffraction data of Mb were processed to a resolution of 2.3 Å based on the criteria of SNR > 1.0 and CC1/2 > 0.4 in the highest-resolution shell (Table 1). Data processing statistics showed that the overall completeness, SNR, CC1/2, and R_{split} were 99.24% (highest-resolution shell: 98.97%), 2.07 (1.22), 0.7261 (0.4101), and 50.27% (82.31%), respectively. Analysis of the Mb XFEL data across resolution ranges indicated that both SNR and CC1/2 were low in the low-resolution region (Figure 2C). This was attributed to the weak diffraction signals of Mb crystals and the relatively high background noise from the XFEL halo during data collection. In addition, these statistics were influenced by the number of merged indexed images. Previous studies demonstrated that increasing the number of diffraction images improves data processing statistics such as completeness, SNR, CC1/2, CC*, and R_{split}, and enhances the quality of structure refinement statistics [54].

To verify whether the data processing results were accurate, MR was performed on the processed XFEL data of Mb. The MR solution yielded top LLG and TFZ scores of 960.605 and 24.5, respectively, indicating that the phase problem was solved. The MR solution was further refined, yielding R_{work} and R_{free} of 27.98% and 35.64%, respectively. The electron density map was clear for model building for main chains from Gly1 to Phe151 (Figure 3A). Further manual inspection of the electron density map and model building were performed according to the electron density map, and most side chains of Mb were well fitted into the electron density map, excluding the side chains of lysine residues. There was no negative Fo–Fc electron density at the iron atom in the heme molecule (Figure 3B), indicating the absence of radiation damage.

Table 1. Data collection statistics of Mb.

Data Collection	Mb
X-ray Source	NCI, PAL-XFEL
Detector	MX225-HS (4 × 4 pixel binning)
XFEL energy (ev)	9500
Pulse width (fs)	~20
Collected images	130,665
Hit images	70,195
Indexed images	1376
Indexed diffraction pattern	1389
Space group	$P2_1$
Cell dimension	
a, b, c (Å)	63.69, 28.62, 35.59
α, β, γ (°)	90.0, 107.16, 90.0
Resolution (Å)	61.72–2.30 (2.38–2.30)
Unique reflections	5781 (577)
Completeness (%)	99.24 (98.97)
Redundancy	11.0 (7.3)
SNR [a]	2.07 (1.22)
CC1/2	0.7261 (0.4101)
CC*	0.917 (0.7627)
$R_{split\ (\%)}$ [b]	50.27 (82.31)
Wilson B-factor (Å^2)	27.66

Values for the outer shell are given in parentheses. [a] SNR, signal-to-noise ratio. [b] $R_{split} = (1/\sqrt{2}) \cdot \frac{\sum_{hkl} |I_{hkl}^{even} - I_{hkl}^{odd}|}{\frac{1}{2} |I_{hkl}^{even} - I_{hkl}^{odd}|}$.

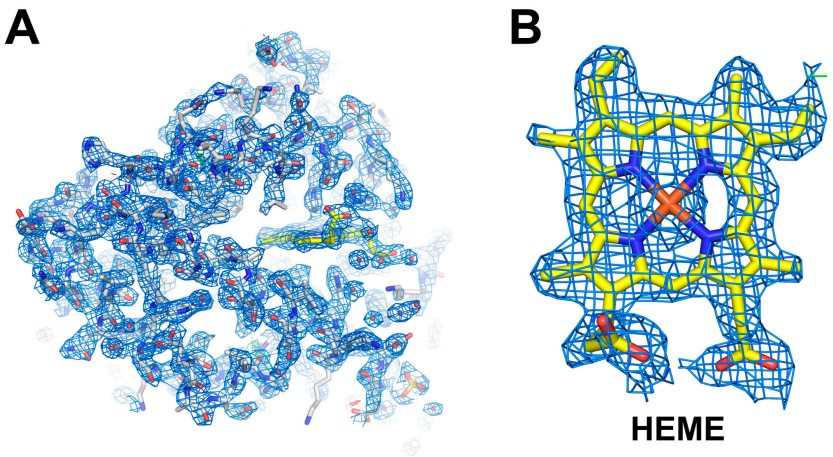


Figure 3. XFEL structure of Mb determined at PAL-XFEL. 2mFo–DFc (blue mesh, 1σ) and mFo–DFc maps (green mesh, +3σ; red mesh, −3σ) for (**A**) the Mb structure and (**B**) the heme molecule bound to Mb.

The B-factors of the heme molecule and the iron atom in the heme were 12.78 and 13.13 Å^2, respectively. These values were lower than those of the protein (16.37 Å^2) and water molecules (18.12 Å^2), indicating that the heme molecule containing the iron atom is rigidly bound to Mb. The final Mb model structure, including 1 heme molecule, 1 sulfate ion, and 54 water molecules, had R_{work} and R_{free} of 24.68% and 31.74%, respectively (Table 2).

The Mb structure collected in this study was compared with two previously reported Mb structures determined in the dark state by SFX (PDB codes: 5CN5 and 8BKH). Superimposition of the Mb structure with Mb-5CN5 and Mb-8BKH yielded RMSDs of 0.266 and 0.239 Å, respectively, revealing identical protein folding and heme-binding positions, whereas the positions of the water molecules defined in the Mb structures slightly differed (Figure 4A). In the superimposed Mb structures, positional differences in the heme

molecules were observed among the XFEL Mb states (Figure 4B). In particular, subtle movements of the residues (Phe43, His64, Val67, Val68, Leu89, His93, His97, Leu104, Ile107, and Phe138) located in the vicinity of the heme molecule were observed (Figure 4C). In the Mb structure determined in this study, there was no reliable electron density map corresponding to any molecule above the iron atom in the heme molecule (Supplementary Figure S1). Conversely, in Mb-5CN5 and Mb-8BKH, a carbon monoxide molecule was located above the heme molecule in Mb (Figure 4C). Therefore, the heme environment of Mb determined in this study differed from those of previously reported Mb structures. In addition, in the XFEL structure of Mb determined in this study, the iron atom in the heme interacted with the NE2 atom of His93 at a distance of 2.33 Å. Meanwhile, the distances between the iron in the heme molecule and the NE2 atom of His93 in Mb-5CN5 and Mb-8BKH were 2.23 and 2.10 Å, respectively. These results indicate that the iron coordination state differs among the Mb structures determined by SFX.

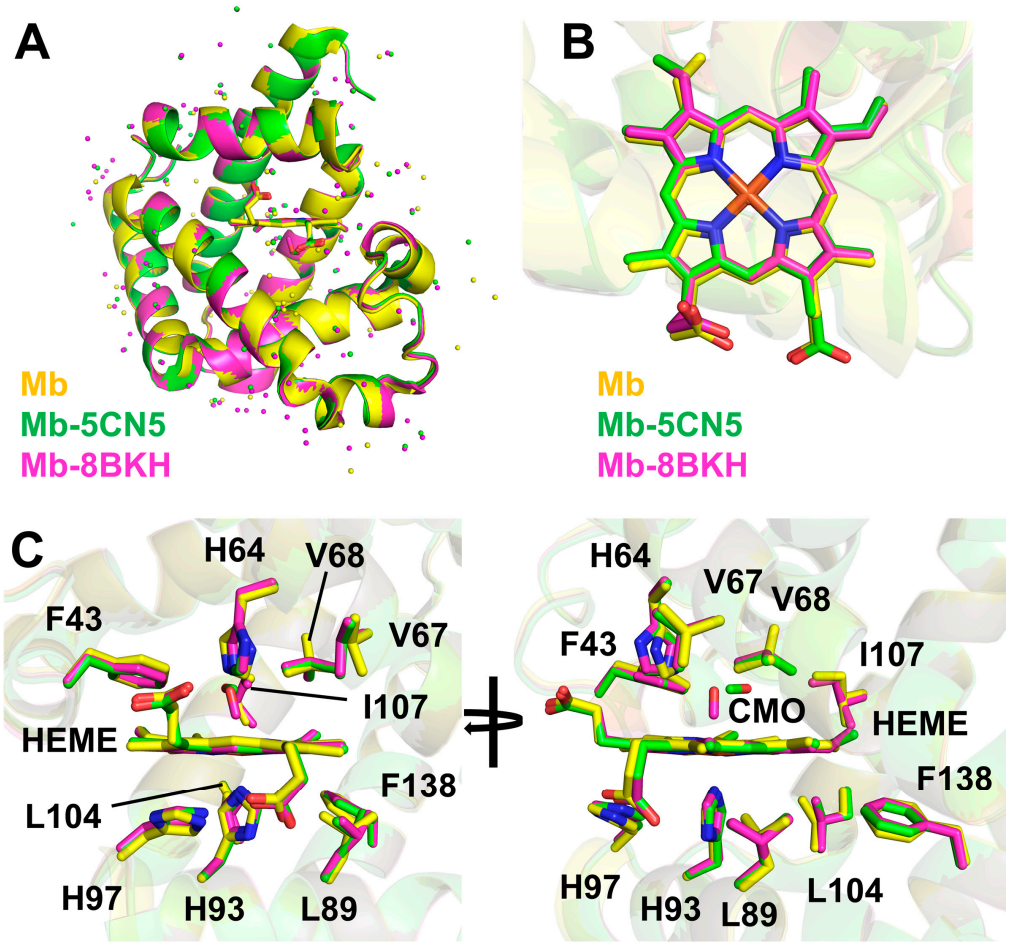


Figure 4. Structural comparison of the Mb structures determined by SFX. (**A**) Superimposition of the Mb structure (yellow) determined in this experiment with previously reported XFEL structures of Mb (PDB codes: 5CN5 [green] and 8BKH [magenta]). (**B**) Comparison of the positions of the heme molecules in the superimposed Mb structures, highlighting subtle positional differences among the heme molecules. (**C**) Close-up view of the residues located in the vicinity of the heme molecule in Mb, revealing subtle differences in side-chain conformation or positioning. In Mb-5CN5 (green) and Mb-8BKH (magenta), a carbon monoxide (CMO) molecule was located on the heme molecule in Mb, whereas no ligand was observed on the heme molecule in Mb determined in this study.

Table 2. Structure solution and refinement statistics of Mb.

Molecular Replacement	Mb
Top LLG	960.605
Top TFZ	24.5
Refinement	
Resolution (Å)	61.42–2.30 (2.53–2.30)
R_{work}	0.2468 (0.2402)
R_{free}	0.3174 (0.3636)
R.m.s.deviation	
Bonds (Å)	0.009
Angles (°)	1.027
Average B factors (Å^2)	
Protein	16.37
Heme	12.24
Water	18.12
Ramachandran plot	
Favored (%)	95.30
Allowed (%)	4.70
PDB code	9X07

Values for the outer shell are given in parentheses.

4. Discussion

Mb plays a critical role in oxygen transport, and structural determination of Mb using XFEL can provide more biologically relevant structural information. In this study, we report XFEL data collection and the initial structural determination of Mb at PAL-XFEL.

A large number of Mb crystals, including both needle-shaped single crystals and needle-like clusters, were obtained by batch crystallization in microtubes. The needle-shaped Mb crystals are suitable for producing single-crystal diffraction patterns, whereas clustered crystals are not ideal for XFEL experiments, as they can generate multiple-crystal diffraction patterns and lead to inaccurate indexing. To avoid multiple-crystal hits from clustered needles, crystallization conditions should be optimized, or alternatively, needle clusters can be physically broken into smaller pieces of appropriate size and shape using a pipette [55].

The high-density Mb crystals were spread onto fixed-target sample holders; however, the overall indexing rate of the XFEL images was low. This was attributed to the weak diffraction signals of Mb crystals, as well as background noise originating from the fixed-target sample holder and the experimental environment. In XFEL images, X-ray scattering rings were observed in the low-resolution region (<10 Å, Figure 2A). An X-ray scattering ring at approximately 14 Å was attributed to background scattering from the polyimide film of the sample holder, whereas other diffuse rings were considered to arise from protein aggregation during crystallization. Therefore, future optimization of Mb crystallization should focus on achieving crystal growth from a clear and soluble protein solution, likely requiring lower protein or precipitant concentrations relative to the current conditions. In addition, the current experiments were performed while exposing the sample holder to ambient air. To further improve the diffraction signal, future data collection should be conducted under a helium atmosphere to avoid background scattering from air.

We successfully solved the phasing problem using 1389 indexed diffraction patterns with MR. This result suggested the possibility of obtaining an interpretable electron density map with fewer than 1400 indexed images, which is significantly lower than the tens of thousands of images typically required for XFEL structure determination. Unlike a previous study in which 956 indexed images were sufficient to solve the phasing problem

for the tetragonal space group of endo-1,4-β-xylanase crystals from *Hypocrea virens* [56], this study demonstrated that in the relatively lower-symmetry monoclinic space group, fewer than 1400 indexed images were adequate for successful phasing. During XFEL data collection, large numbers of diffraction images are spontaneously generated because of the high repetition rate of XFEL. Thus, the ability to evaluate data quality and assess the feasibility of structure determination with approximately 1000 indexed images is of practical importance. Meanwhile, additional XFEL data collection and processing of Mb will enable the current dataset to be merged with future datasets to obtain a complete high-quality structure.

The Mb structure determined in this study was compared with two previously reported Mb structures determined by SFX (PDB codes: 5CN5 and 8BKH), revealing subtle differences in the Mb structure, including the heme environment. However, in this study, Mb was not maintained in specific functional states such as oxy-Mb or deoxy-Mb. Accordingly, direct structural comparison might not be possible. Nevertheless, these structural differences could be useful for understanding the structural flexibility of the Mb molecule. To more accurately clarify the molecular function of Mb, future SFX studies should include high-resolution structure determination and careful sample preparation under state-specific conditions.

Taken together, these results demonstrate that Mb crystallization, XFEL data processing, and structure determination were successfully achieved, and a validated workflow was established for future rapid structure determination at PAL-XFEL.

Supplementary Materials: The following supporting information can be downloaded at: https://www.mdpi.com/article/10.3390/cryst15100905/s1, Figure S1: Electron-density map of the heme environment in Mb.

Author Contributions: Conceptualization, K.H.N.; methodology, S.P., J.P. and K.H.N.; formal analysis, K.H.N.; investigation, S.P., J.P. and K.H.N.; data curation, S.P. and J.P.; writing—original draft preparation, K.H.N.; writing—review and editing, S.P. and J.P.; visualization, K.H.N. All authors have read and agreed to the published version of the manuscript.

Funding: This work was funded by the National Research Foundation of Korea (NRF) (NRF-2021R1I1A1A01050838). Experiments at PAL-XFEL were supported in part by MSIT and POSTECH (XFEL2025-01). This study was supported by Kookmin University.

Data Availability Statement: The structure factor and coordinates of Mb were deposited at the Protein Data Bank (https://www.rcsb.org) under access code 9X07.

Acknowledgments: We thank the beamline staff at PAL-XFEL at Pohang Accelerator Laboratory for their assistance with data collection. The authors thank the Global Science experimental Data hub Center (GSDC) at the Korea Institute of Science and Technology Information (KISTI) for providing computing resources and technical support. The XFEL experiments were carried out at the NCI endstation at PAL-XFEL (Proposal No. 2025-2nd-NCI-I002).

Conflicts of Interest: The authors declare no conflicts of interest.

Abbreviations

The following abbreviations are used in this manuscript:

Mb	Myoglobin
SFX	Serial Femtosecond Crystallography
XFEL	X-ray Free Electron Laser

References

1. Wittenberg, B.A.; Wittenberg, J.B. Myoglobin-mediated oxygen delivery to mitochondria of isolated cardiac myocytes. *Proc. Natl. Acad. Sci. USA* **1987**, *84*, 7503–7507. [CrossRef]
2. Gros, G.; Wittenberg, B.A.; Jue, T. Myoglobin's old and new clothes: From molecular structure to function in living cells. *J. Exp. Biol.* **2010**, *213*, 2713–2725. [CrossRef]
3. Wittenberg, J.B.; Wittenberg, B.A. Myoglobin function reassessed. *J. Exp. Biol.* **2003**, *206*, 2011–2020. [CrossRef]
4. Kendrew, J.C.; Dickerson, R.E.; Strandberg, B.E.; Hart, R.G.; Davies, D.R.; Phillips, D.C.; Shore, V.C. Structure of Myoglobin: A Three-Dimensional Fourier Synthesis at 2 Å. Resolution. *Nature* **1960**, *185*, 422–427. [CrossRef]
5. Carlsson, M.L.R.; Kanagarajan, S.; Bülow, L.; Zhu, L.-H. Plant based production of myoglobin—A novel source of the muscle heme-protein. *Sci. Rep.* **2020**, *10*, 920. [CrossRef] [PubMed]
6. Qian, Y.; Liang, G.; Dong, J.; Zhou, J.; Li, J.; Chen, J.; Du, G.; Chen, J.; Wang, Z.; Zhao, X. Effect of myoglobin on the flavor, color and texture of high-moisture soy protein concentrate -wheat gluten extrudates. *Food Chem.* **2025**, *473*, 143102. [CrossRef] [PubMed]
7. Plebani, M.; Zaninotto, M. Diagnostic strategies using myoglobin measurement in myocardial infarction. *Clin. Chim. Acta* **1998**, *272*, 69–77. [CrossRef] [PubMed]
8. Vojtěchovský, J.; Chu, K.; Berendzen, J.; Sweet, R.M.; Schlichting, I. Crystal Structures of Myoglobin-Ligand Complexes at Near-Atomic Resolution. *Biophys. J.* **1999**, *77*, 2153–2174. [CrossRef]
9. Postnikova, G.B.; Shekhovtsova, E.A. Myoglobin: Oxygen Depot or Oxygen Transporter to Mitochondria? A Novel Mechanism of Myoglobin Deoxygenation in Cells (review). *Biochemistry* **2018**, *83*, 168–183. [CrossRef]
10. Strandberg, B. Chapter 1: Building the Ground for the First Two Protein Structures: Myoglobin and Haemoglobin. *J. Mol. Biol.* **2009**, *392*, 2–10. [CrossRef]
11. Brunori, M.; Bourgeois, D.; Vallone, B. The structural dynamics of myoglobin. *J. Struct. Biol.* **2004**, *147*, 223–234. [CrossRef]
12. Kaieda, S.; Halle, B. Internal Water and Microsecond Dynamics in Myoglobin. *J. Phys. Chem. B* **2013**, *117*, 14676–14687. [CrossRef]
13. Kern, D.; Zuiderweg, E.R.P. The role of dynamics in allosteric regulation. *Curr. Opin. Struct. Biol.* **2003**, *13*, 748–757. [CrossRef]
14. de Chadarevian, S. John Kendrew and myoglobin: Protein structure determination in the 1950s. *Protein Sci.* **2018**, *27*, 1136–1143. [CrossRef] [PubMed]
15. Nam, K.H. Radiation Damage on Thaumatin: A Case Study of Crystals That Are Larger Than the Microfocusing X-ray Beam. *Appl. Sci.* **2023**, *13*, 1876. [CrossRef]
16. Nam, K.H. Radiation Damage on Selenomethionine-Substituted Single-Domain Substrate-Binding Protein. *Crystals* **2023**, *13*, 1620. [CrossRef]
17. Nam, K.H. Guide to serial synchrotron crystallography. *Curr. Res. Struct. Biol.* **2024**, *7*, 100131. [CrossRef]
18. Nam, K.H. Temperature-Dependent Structural Changes of the Active Site and Substrate-Binding Cleft in Hen Egg White Lysozyme. *Crystals* **2025**, *15*, 111. [CrossRef]
19. Garman, E.F. Radiation damage in macromolecular crystallography: What is it and why should we care? *Acta Crystallogr. D Biol. Crystallogr.* **2010**, *66*, 339–351. [CrossRef] [PubMed]
20. Shelley, K.L.; Garman, E.F. Quantifying and comparing radiation damage in the Protein Data Bank. *Nat. Commun.* **2022**, *13*, 1314. [CrossRef]
21. Pfanzagl, V.; Beale, J.H.; Michlits, H.; Schmidt, D.; Gabler, T.; Obinger, C.; Djinović-Carugo, K.; Hofbauer, S. X-ray–induced photoreduction of heme metal centers rapidly induces active-site perturbations in a protein-independent manner. *J. Biol. Chem.* **2020**, *295*, 13488–13501. [CrossRef]
22. Della Longa, S.; Arcovito, A.; Benfatto, M.; Congiu-Castellano, A.; Girasole, M.; Hazemann, J.L.; Lo Bosco, A. Redox-Induced Structural Dynamics of Fe-Heme Ligand in Myoglobin by X-Ray Absorption Spectroscopy. *Biophys. J.* **2003**, *85*, 549–558. [CrossRef]
23. Boutet, S.; Lomb, L.; Williams, G.J.; Barends, T.R.M.; Aquila, A.; Doak, R.B.; Weierstall, U.; DePonte, D.P.; Steinbrener, J.; Shoeman, R.L.; et al. High-Resolution Protein Structure Determination by Serial Femtosecond Crystallography. *Science* **2012**, *337*, 362–364. [CrossRef]
24. Barends, T.R.M.; Stauch, B.; Cherezov, V.; Schlichting, I. Serial femtosecond crystallography. *Nat. Rev. Methods Primers* **2022**, *2*, 59. [CrossRef] [PubMed]
25. Chapman, H.N.; Caleman, C.; Timneanu, N. Diffraction before destruction. *Philos. Trans. R. Soc. B Biol. Sci.* **2014**, *369*, 20130313. [CrossRef] [PubMed]
26. Neutze, R.; Wouts, R.; van der Spoel, D.; Weckert, E.; Hajdu, J. Potential for biomolecular imaging with femtosecond X-ray pulses. *Nature* **2000**, *406*, 752–757. [CrossRef] [PubMed]
27. Orville, A.M. Recent results in time resolved serial femtosecond crystallography at XFELs. *Curr. Opin. Struct. Biol.* **2020**, *65*, 193–208. [CrossRef]
28. Park, J.; Nam, K.H. Recent chemical mixing devices for time-resolved serial femtosecond crystallography. *TrAC Trends Anal. Chem.* **2024**, *172*, 117554. [CrossRef]

29. Park, J.; Nam, K.H. Experimental approaches for time-resolved serial femtosecond crystallography at PAL-XFEL. In *Time-Resolved Methods in Structural Biology*; Methods in Enzymology; Academic Press: Cambridge, MA, USA, 2024; pp. 131–160.
30. Barends, T.R.M.; Foucar, L.; Ardevol, A.; Nass, K.; Aquila, A.; Botha, S.; Doak, R.B.; Falahati, K.; Hartmann, E.; Hilpert, M.; et al. Direct observation of ultrafast collective motions in CO myoglobin upon ligand dissociation. *Science* **2015**, *350*, 445–450. [CrossRef]
31. Barends, T.R.M.; Gorel, A.; Bhattacharyya, S.; Schirò, G.; Bacellar, C.; Cirelli, C.; Colletier, J.-P.; Foucar, L.; Grünbein, M.L.; Hartmann, E.; et al. Influence of pump laser fluence on ultrafast myoglobin structural dynamics. *Nature* **2024**, *626*, 905–911. [CrossRef]
32. Oghbaey, S.; Sarracini, A.; Ginn, H.M.; Pare-Labrosse, O.; Kuo, A.; Marx, A.; Epp, S.W.; Sherrell, D.A.; Eger, B.T.; Zhong, Y.; et al. Fixed target combined with spectral mapping: Approaching 100% hit rates for serial crystallography. *Acta Crystallogr. D Struct. Biol.* **2016**, *72*, 944–955. [CrossRef]
33. Owen, R.L.; Axford, D.; Sherrell, D.A.; Kuo, A.; Ernst, O.P.; Schulz, E.C.; Miller, R.J.; Mueller-Werkmeister, H.M. Low-dose fixed-target serial synchrotron crystallography. *Acta Crystallogr. D Struct. Biol.* **2017**, *73*, 373–378. [CrossRef]
34. Calvey, G.D.; Katz, A.M.; Zielinski, K.A.; Dzikovski, B.; Pollack, L. Characterizing Enzyme Reactions in Microcrystals for Effective Mix-and-Inject Experiments using X-ray Free-Electron Lasers. *Anal. Chem.* **2020**, *92*, 13864–13870. [CrossRef]
35. Mehrabi, P.; Bücker, R.; Bourenkov, G.; Ginn, H.M.; von Stetten, D.; Müller-Werkmeister, H.M.; Kuo, A.; Morizumi, T.; Eger, B.T.; Ou, W.L.; et al. Serial femtosecond and serial synchrotron crystallography can yield data of equivalent quality: A systematic comparison. *Sci. Adv.* **2021**, *7*, eabf1380. [CrossRef]
36. Brucker, E.A.; Olson, J.S.; Phillips, G.N.; Dou, Y.; Ikeda-Saito, M. High Resolution Crystal Structures of the Deoxy, Oxy, and Aquomet Forms of Cobalt Myoglobin. *J. Biol. Chem.* **1996**, *271*, 25419–25422. [CrossRef]
37. Deng, Y.; Albert, T.; Van Stappen, C.; Palacios, P.M.; Amador, M.L.; Dwaraknath, S.; Guo, Y.; Moënne-Loccoz, P.; Lu, Y. Unveiling an Ultrareduced State of Heme in Myoglobin. *J. Am. Chem. Soc.* **2025**, *147*, 29983–29993. [CrossRef]
38. Nam, K.H. Real-time monitoring of large-scale crystal growth using batch crystallization for serial crystallography. *J. Cryst. Growth* **2023**, *614*, 127219. [CrossRef]
39. Lee, D.; Baek, S.; Park, J.; Lee, K.; Kim, J.; Lee, S.J.; Chung, W.K.; Lee, J.L.; Cho, Y.; Nam, K.H. Nylon mesh-based sample holder for fixed-target serial femtosecond crystallography. *Sci. Rep.* **2019**, *9*, 6971. [CrossRef] [PubMed]
40. Park, J.; Kim, S.; Nam, K.H.; Kim, B.; Ko, I.S. Current status of the CXI beamline at the PAL-XFEL. *J. Korean Phys. Soc.* **2016**, *69*, 1089–1093. [CrossRef]
41. Kang, H.S.; Min, C.K.; Heo, H.; Kim, C.; Yang, H.; Kim, G.; Nam, I.; Baek, S.Y.; Choi, H.J.; Mun, G.; et al. Hard X-ray free-electron laser with femtosecond-scale timing jitter. *Nat. Photonics* **2017**, *11*, 708–713. [CrossRef]
42. Kim, J.; Kim, H.Y.; Park, J.; Kim, S.; Kim, S.; Rah, S.; Lim, J.; Nam, K.H. Focusing X-ray free-electron laser pulses using Kirkpatrick-Baez mirrors at the NCI hutch of the PAL-XFEL. *J. Synchrotron Radiat.* **2018**, *25*, 289–292. [CrossRef]
43. Mariani, V.; Morgan, A.; Yoon, C.H.; Lane, T.J.; White, T.A.; O'Grady, C.; Kuhn, M.; Aplin, S.; Koglin, J.; Barty, A.; et al. OnDA: Online data analysis and feedback for serial X-ray imaging. *J. Appl. Crystallogr.* **2016**, *49*, 1073–1080. [CrossRef]
44. Barty, A.; Kirian, R.A.; Maia, F.R.; Hantke, M.; Yoon, C.H.; White, T.A.; Chapman, H. Cheetah: Software for high-throughput reduction and analysis of serial femtosecond X-ray diffraction data. *J. Appl. Crystallogr.* **2014**, *47*, 1118–1131. [CrossRef]
45. White, T.A. Processing serial crystallography data with CrystFEL: A step-by-step guide. *Acta Crystallogr. D Struct. Biol.* **2019**, *75*, 219–233. [CrossRef]
46. Gevorkov, Y.; Yefanov, O.; Barty, A.; White, T.A.; Mariani, V.; Brehm, W.; Tolstikova, A.; Grigat, R.R.; Chapman, H.N. XGANDALF—Extended gradient descent algorithm for lattice finding. *Acta Crystallogr. A Found. Adv.* **2019**, *75*, 694–704. [CrossRef]
47. Yefanov, O.; Mariani, V.; Gati, C.; White, T.A.; Chapman, H.N.; Barty, A. Accurate determination of segmented X-ray detector geometry. *Opt. Express* **2015**, *23*, 28459–28470. [CrossRef]
48. Liebschner, D.; Afonine, P.V.; Baker, M.L.; Bunkoczi, G.; Chen, V.B.; Croll, T.I.; Hintze, B.; Hung, L.W.; Jain, S.; McCoy, A.J.; et al. Macromolecular structure determination using X-rays, neutrons and electrons: Recent developments in Phenix. *Acta Crystallogr. D Struct. Biol.* **2019**, *75*, 861–877. [CrossRef] [PubMed]
49. Maurus, R.; Bogumil, R.; Nguyen, N.T.; Mauk, A.G.; Brayer, G. Structural and spectroscopic studies of azide complexes of horse heart myoglobin and the His-64→Thr variant. *Biochem. J.* **1998**, *332*, 67–74. [CrossRef] [PubMed]
50. Emsley, P.; Cowtan, K. Coot: Model-building tools for molecular graphics. *Acta Crystallogr. D Biol. Crystallogr.* **2004**, *D60*, 2126–2132. [CrossRef] [PubMed]
51. Williams, C.J.; Headd, J.J.; Moriarty, N.W.; Prisant, M.G.; Videau, L.L.; Deis, L.N.; Verma, V.; Keedy, D.A.; Hintze, B.J.; Chen, V.B.; et al. MolProbity: More and better reference data for improved all-atom structure validation. *Protein Sci.* **2018**, *27*, 293–315. [CrossRef]
52. Gevorkov, Y.; Barty, A.; Brehm, W.; White, T.A.; Tolstikova, A.; Wiedorn, M.O.; Meents, A.; Grigat, R.-R.; Chapman, H.N.; Yefanov, O. pinkIndexer—A universal indexer for pink-beam X-ray and electron diffraction snapshots. *Acta Crystallogr. A Found. Adv.* **2020**, *76*, 121–131. [CrossRef] [PubMed]

53. Beyerlein, K.R.; White, T.A.; Yefanov, O.; Gati, C.; Kazantsev, I.G.; Nielsen, N.F.-G.; Larsen, P.M.; Chapman, H.N.; Schmidt, S. FELIX: An algorithm for indexing multiple crystallites in X-ray free-electron laser snapshot diffraction images. *J. Appl. Crystallogr.* **2017**, *50*, 1075–1083. [CrossRef]
54. Nam, K.H. Impact of Diffraction Data Volume on Data Quality in Serial Crystallography. *Crystals* **2025**, *15*, 104. [CrossRef]
55. Park, J.; Park, S.; Kim, J.; Park, G.; Cho, Y.; Nam, K.H. Polyacrylamide injection matrix for serial femtosecond crystallography. *Sci. Rep.* **2019**, *9*, 2525. [CrossRef] [PubMed]
56. Nam, K.H.; Park, S.; Park, J. Preliminary XFEL data from spontaneously grown endo-1,4-β-xylanase crystals from *Hypocrea virens*. *Acta Crystallogr. F Struct. Biol. Commun.* **2022**, *78*, 226–231. [CrossRef] [PubMed]

Disclaimer/Publisher's Note: The statements, opinions and data contained in all publications are solely those of the individual author(s) and contributor(s) and not of MDPI and/or the editor(s). MDPI and/or the editor(s) disclaim responsibility for any injury to people or property resulting from any ideas, methods, instructions or products referred to in the content.